The Sensitivity of an Idealized Weddell Gyre to Horizontal Resolution

Andrew F. Styles[1], Michael J. Bell[2], David P. Marshall[1]

[1]Department of Physics, University of Oxford, Oxford, UK
[2]Met Office, Fitzroy Road, Exeter, UK

Key Points:

- An idealized model of the Weddell Gyre demonstrates that the gyre can be extremely sensitive to horizontal resolution.
- The gyre is strongest at eddy-permitting resolutions where the meridional density gradients are largest and the stratification is weakest.
- The depth-varying component of the Weddell Gyre is controlled by the density structure and the bottom flow is sensitive to explicit eddies.

Corresponding author: Andrew F. Styles, afstylesocean@gmail.com

Abstract

Estimates of the Weddell Gyre transport vary widely between climate simulations. Here, we investigate if inter-model variability can originate from differences in the horizontal resolution of the ocean model. We run an idealized model of the Weddell Gyre at eddy-parametrized, eddy-permitting, and eddy-rich resolutions and find that the gyre is very sensitive to horizontal resolution and the gyre transport is largest at eddy-permitting resolutions. The eddy-permitting simulations have the largest horizontal density gradients and the weakest stratification over the gyre basin. The large horizontal density gradients induce a significant thermal wind transport and increase the mean available potential energy for mesoscale eddies. Explicit eddies in simulations intensify the bottom circulation of the gyre via non-linear dynamics. If climate models adopt horizontal resolutions that the Weddell Gyre is most sensitive to, then simulations of the Weddell Gyre could become more disparate.

Plain Language Summary

The Weddell Gyre is a large horizontal circulation in the southern hemisphere which is exposed to very low atmospheric temperatures and lies under extensive sea ice. Extremely dense water forms in the Weddell Sea, which the Weddell Gyre exports to the global ocean. These exported dense water masses change the Earth's climate by altering the total heat and carbon content in the global ocean. Between climate simulations, the volume of water transported by the Weddell Gyre varies significantly: we investigate if this variability can originate from differences in the horizontal spatial resolution of the ocean models. Using a simplified model of the Weddell Gyre, we find that the intensity of the circulation is extremely sensitive to the horizontal resolution. The circulation is particularly strong at intermediate resolutions, where only the largest ocean eddies are resolved. At intermediate resolutions, horizontal density gradients are the largest and the vertical density gradients are the smallest; this unique density structure allows for a particularly strong Weddell Gyre circulation. These results have important implications for long-range ocean climate projections.

1 Introduction

The Weddell Gyre is the largest subpolar gyre in the southern hemisphere which spans an area of approximately six million square kilometers in the Atlantic sector of the Southern Ocean. Buoyancy forcing in this region is intense as atmospheric temperatures are low and sea ice formation is extensive. The Weddell Gyre also lies immediately south of the Antarctic Circumpolar Current (ACC), the strongest current in the global ocean.

Extremely dense water masses are produced in the Weddell Gyre as small bodies of water are exposed to intense buoyancy forcing for a prolonged period of time. Of particular interest is the production and export of Antarctic Bottom Water (AABW), which contributes to the southern closure of the global overturning circulation when exported northwards (J. Marshall & Speer, 2012). The Weddell Gyre strength can control the variability of dense water export (Meijers et al., 2016) and could potentially influence global overturning. It should be noted that there is some debate about exactly how much AABW is produced and exported by the Weddell Gyre. Orsi et al. (1999, 2002) suggest upwards of 60-70% of all AABW originates from the Weddell Gyre while Jullion et al. (2014) argues that such high estimates are overstated as they find that up to 30% of the AABW exported by the gyre is recycled from the Southern Ocean Indian Sector.

The surrounding coastline and local topographic features shape the Weddell Gyre, as seen in Figure 1a. The southern limb of the gyre follows the border of the Antarctic mainland and the the western limb is steered north by the Antarctic Peninsula. It is uncertain whether any topographic feature constrains the eastern boundary of the Weddell Gyre as estimates of the the eastern boundary location range from 30°E (Deacon, 1979) to as far as 70°E (Park et al., 2001). Within this longitudinal range there is an abundance of eddies that allow exchange between the gyre and ACC (Schröder & Fahrbach, 1999; Park et al., 2001; Ryan et al., 2016).

Two zonally-elongated ridges act as partial barriers between the ACC and Weddell Gyre: the South Scotia Ridge in the west and the North Weddell Ridge in the east (Vernet et al., 2019). These ridge systems are typically within 1500 to 2000 m of the sea surface and are very steep in places. Submarine ridges block deep currents from crossing the ACC-gyre interface and play a major role in setting the stratification across the entire region (Orsi et al., 1993; Wilson et al., 2022). Figures 1b and 1c are hydrographic sections of the Weddell Gyre and ACC showing potential temperature and salinity respectively. The contours of potential temperature and salinity in the Weddell Gyre are domed and consequently there is a steep meridional density gradient above the submarine ridge (approx. 54°S in Figures 1b and c). As a result, only the densest components of the circumpolar flow are exposed to the intense buoyancy forcing found near the sea surface of the Weddell basin and on the continental shelf.

Measurements of the Weddell Gyre transport are limited and vary widely. Gordon et al. (1981) uses wind stress data and applies Sverdrup balance to estimate the Weddell Gyre transport as 76 Sv (1 Sv $= 10^6$ m^{3}s^{-1}) while questioning the validity of Sverdrup dynamics. Moorings and ship data provide lower estimates of the transport, for example, 20-56 Sv from Fahrbach et al. (1991) and 30 Sv from Yaremchuk et al. (1998). In Reeve et al. (2019), the Weddell Gyre transport is estimated to be 32 $\pm$ 5 Sv using Argo data (Argo, 2020). Although recent Argo data have significantly increased the number of available observations, coverage is still fairly limited. Argo data has contributed approximately 1500 data points (south of 60°S) over a time period of 14 years with no measurements taken below 2000 dbar. Reeve et al. (2019) uses the thermal wind relation to estimate the geostrophic velocity in the upper 2000 dbar of the Weddell Gyre and extrapolates over depth to estimate the full volume transport while relying on ship-based observations to estimate the extrapolation error.

Climate models disagree on the strength and shape of the Weddell Gyre and limited winter-time observations make it difficult to assess model accuracy in this region. Wang (2013) studies fourteen CMIP5 simulations with horizontal resolutions of 1° or coarser and finds that the time-averaged Weddell Gyre transport ranges from approximately 10 to 80 Sv. This is troubling as Meijers et al. (2016) suggests that variability in the export of dense Weddell Sea slope water is closely tied to wind-driven acceleration of the Weddell Gyre's western boundary current. Inconsistent Weddell Gyre circulations between climate models may lead to inconsistent descriptions of the global overturning circulation and consequently inconsistent global heat, carbon, and freshwater budgets.

Long time integrations of numerical ocean models under different climate forcing scenarios are prohibitively expensive to run at mesoscale eddy-resolving resolutions, but high resolution simulations are becoming increasingly affordable. Hewitt et al. (2020) comments that the average horizontal resolution of the ocean has increased with each iteration of CMIP and this corresponds to an approximate doubling of horizontal resolution every ten years (Fox-Kemper, 2018). The majority of centres participating in CMIP6 parametrize the effect of unresolved eddies, but there are now several 'eddy-permitting' models that at least partially resolve the mesoscale eddies, taking into account the small Rossby deformation radius at these high latitudes (LaCasce & Groeskamp, 2020).

In the idealized and eddy-permitting simulations by Wilson et al. (2022), it is noted that the introduction of a zonal submarine ridge intensifies the Weddell Gyre. Wilson also comments that the ACC and Weddell Gyre primarily interact through transient eddies on the eastern boundary of the zonal ridge. In this article, we aim to investigate how

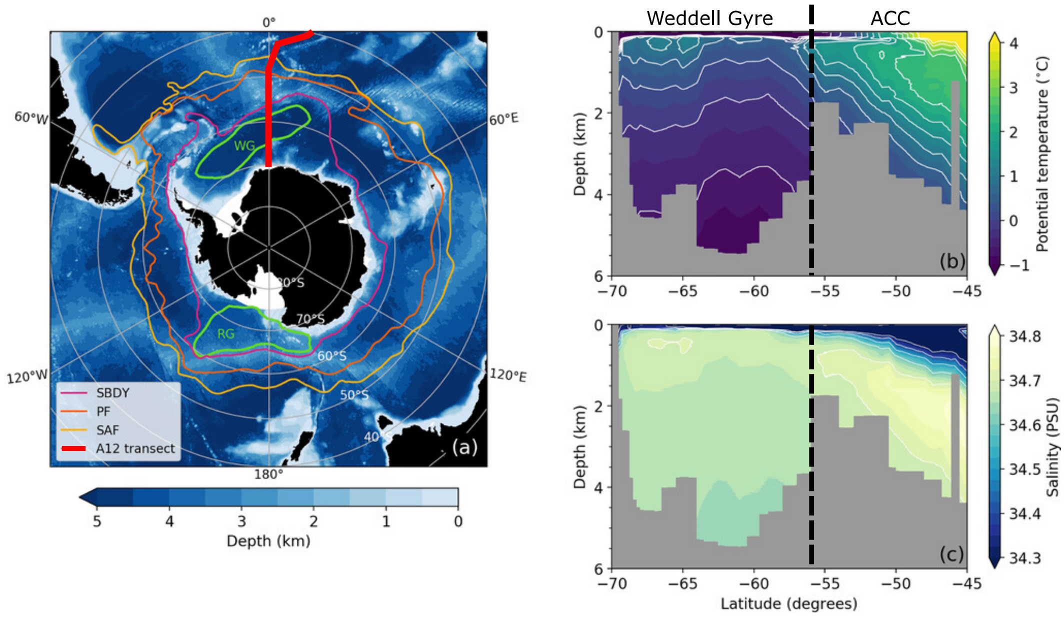

Figure 1. Reproduced from Wilson et al. (2022), bathymetric and hydrographic features of the Southern Ocean. (a) Bathymetry of the Southern Ocean, contours mark three fronts of the ACC (Orsi et al., 1995): Southern Boundary (SBDY), Polar Front (PF), and Subantarctic Front (SAF). Outlines of the Weddell Gyre (WG) and and Ross Gyre (RG) are also shown, using contours of satellite-based dynamic ocean topography (Armitage et al., 2018). (b) and (c) are hydrographic sections of potential temperature and salinity through the Weddell Sea along the A12 transect [red line in (a)]. These hydrographic data were collected by the R/V Polarstern during the 1992 ANT/X research cruise.

model resolution influences the Weddell Gyre and its interaction with the ACC. This is addressed using an idealized model that builds on Wilson et al. (2022). The model is run at a wide range of horizontal resolutions including: eddy-parametrized scales (80 and 40 km), eddy-permitting scales (10 and 20 km), and finally at an eddy-rich scale (3 km). The Weddell Gyre is found to be extremely sensitive to horizontal resolution and is strongest at eddy-permitting resolutions.

The article is structured as follows. In Section 2 we describe the idealized model used in this study and in Section 3 we describe the three experiments that are carried out. In Section 4 we present our results including a thermal wind decomposition of the Weddell Gyre and ACC transport. In Section 5, we discuss how explicit eddies can strengthen the flow at the sea floor and the missing physics in our model design. Closing remarks are made in Section 6.

2 Model design

The experiments presented in this article are performed in the NEMO Community Ocean model (Madec et al., 2019) in a configuration that is similar to the model used by Wilson et al. (2022). The configuration features a zonally periodic channel and a southern continental shelf which resembles the neighbouring coastline for the Weddell Gyre (see Figure 2a). Two large landmasses are present on the western margins of the model, with an opening that crudely represents the Drake Passage. Additional topographic features include a submarine ridge which extends eastwards from the idealized Drake Pas-

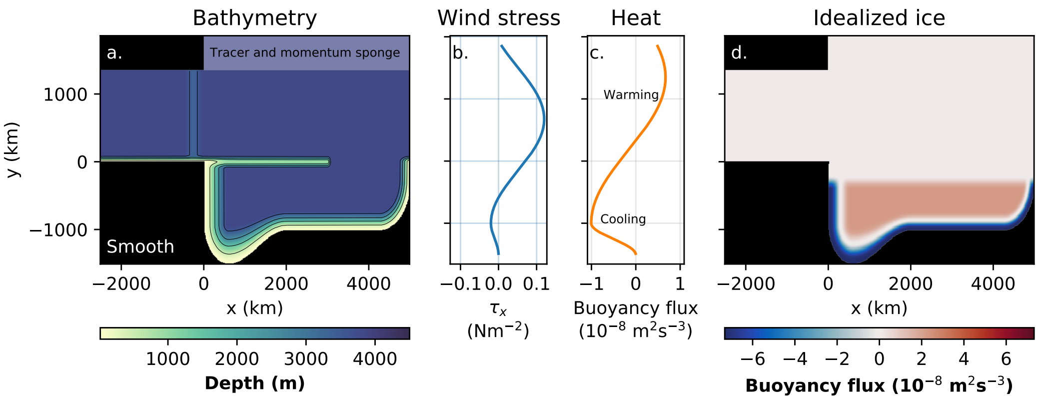

Figure 2. Summary of the model configuration. (a) Bathymetry of the model (without topographic noise) with contours at 1000 m intervals. (b) The zonal wind stress profile for the configuration. (c) The zonal heat flux profile for the configuration in units of buoyancy flux. (d) The freshwater fluxes used to represent sea ice for the configuration in units of buoyancy flux. In this model, a buoyancy flux of 10^{-8} m^{2}s^{-3} corresponds to 14.9 Wm^{-2} of surface heating or approximately $4{\times}10^{-5}$ kg m^{-2}s^{-1} of freshwater input (dependent on surface salinity).

sage and a meridional sill in the Drake Passage that blocks f/H contours and regulates the ACC transport (f is the Coriolis parameter and H is the ocean depth). The parameters for these topographic features and all other relevant fixed parameters can be found in Table 1. Throughout this article, the x coordinate is the zonal displacement from the eastern boundary of the Drake Passage and the y coordinate is the meridional displacement from the southern boundary of the Drake Passage (see axes in Figure 2a).

The model has a regular horizontal grid with a horizontal grid space between 80 and 3 km, depending on the experiment (see Table 2). All configurations use z-coordinates and have 31 vertical model levels, with vertical spacing that is approximately 10 m near the sea surface, 315 m near the sea floor, and partial cells are used to represent the varying sea floor. The configuration exists on a beta plane where the Coriolis parameter varies linearly with the meridional coordinate, y, around its value at 65°S (y=0 in Figure 2). The model uses a free slip condition on lateral boundaries and applies a linear friction to the bottom boundary. A simplified linear equation of state is used with a thermal expansion coefficient of $a_0 = 2.8{\times}10^{-4}$ kg m^{-3} K^{-1} and a haline coefficient of $b_0 = 7.7\times 10^{-4}$ kg m^{-3} psu^{-1}. When using a linear equation of state, there is no distinction between conservative and potential temperature, nor is there a distinction between absolute and practical salinity; therefore, in our results we will simply refer to temperature and salinity. The horizontal diffusion of momentum and tracers is implemented with a diffusivity that scales linearly with horizontal resolution (see Table 1).

The model is forced with a sinusoidal and zonal wind stress which only varies in the meridional direction. The wind stress profile resembles the zonally and annually averaged wind stress across the Southern Ocean (Figure 2b), with a maximum westerly wind stress of 0.12 N m^{-2} over the center of the circumpolar channel and a peak easterly wind stress of 0.02 N m^{-2} along the continental shelf. Similarly, the surface heat flux is also sinusoidal and zonally uniform with a maximum surface warming of 10 Wm^{-2} at the northern boundary of the Drake Passage and a peak cooling of 15 W m^{-2} on the south continental shelf. The surface heat flux is shown in units of buoyancy flux in Figure 2c.

Table 1. Summary of fixed parameters in the model. Δx is the horizontal grid spacing of the model in meters. (*) The sill height is varied for the ACC sensitivity experiment but is 500 m for all other experiments.

Model parameter	Value
Meridional domain size	3350 km
Zonal domain size	7520 km
Reference Coriolis parameter	1.3×10^{-4} s^{-1}
Meridional gradient of Coriolis parameter	9.6×10^{-12} s^{-1}m^{-1}
Momentum diffusivity (resolution dependent)	0.05 Δx m^2 s^{-1}
Tracer diffusivity (resolution dependent)	0.005 Δx m^2 s^{-1}
Maximum (smooth) ocean depth	4000 m
Number of model levels	31
Vertical resolution	10 - 315 m
Continental shelf width	300 - 600 km
Drake Passage zonal length	2520 km
Drake Passage meridional width size	1350 km
Drake passage sill zonal width	500 km
Drake passage sill maximum height*	500 m
Submarine ridge zonal extent	3000 km
Submarine ridge meridional width	200 km
Submarine ridge maximum height	3000 m
Root mean square of topographic noise	100 m
Topographic noise length scales	240, 120, 60, 30, 9 km
Topographic noise relative amplitudes	8, 4, 2, 1, 0.3

The effect of sea ice on the salinity budget is simply represented by a surface freshwater flux, as shown in units of buoyancy flux in Figure 2d. The freshwater fluxes resemble the annual-average freshwater fluxes due to sea ice in the Southern Ocean, with net freshwater release in the Weddell basin and persistent sea ice formation on the southern continental shelf. Freshwater fluxes are the dominant buoyancy flux in the Weddell basin, as argued by Pellichero et al. (2018), but they do not extend onto the submarine ridge in the idealized model. The domain area integral of freshwater fluxes is identically zero to conserve the water content of the model.

The northern margin of the model ($y > 1350$ km) contains a sponge layer, which parameterizes the effect of the global ocean to the north. The horizontal flow is relaxed to rest, the salinity is relaxed to 35 psu at all depths, and the temperature is relaxed to the vertical profile,

$$T(z) = T_{\text{top}} exp(z/\delta_z), \tag{1}$$

where T is the temperature, z is the vertical coordinate, $T_{\text{top}} = 10$°C is the prescribed sea surface temperature and $\delta_z = 1500$ m is the decay length scale of the surface temperature. Consequently, the prescribed sea floor temperature is approximately 0°C. The momentum sponge has a relaxation timescale of approximately 10 days and the tracer sponge has a relaxation timescale of approximately 100 days and the sponge layer is 500 km wide.

In some experiments (see the next section) topographic noise is introduced to the bathymetry, as shown in Figure 3. The addition of weak topographic noise permits topographic interactions everywhere in the domain but only perturbs the larger scale bathymetric features. The analytic noise field is generated using a zonally periodic and continuous noise generation function, $\mathcal{O}(x, y)$, from OpenSimplex (Spencer, 2022). Noise is

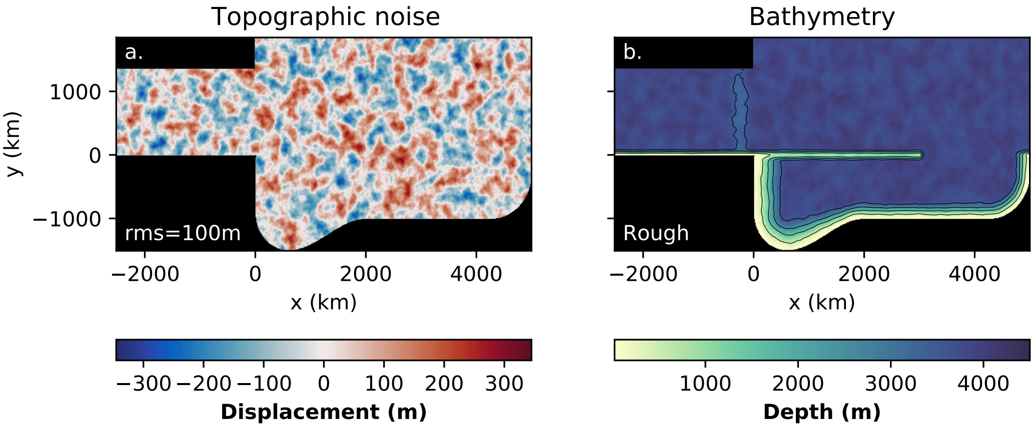

Figure 3. (a) Noise profile and (b) bathymetry for the Rough simulation with a horizontal resolution of 3 km. All discrete noise fields used in this article have a root mean square of 100 m and are based on the same continuous noise function, $\mathcal{O}(x, y)$.

added at various length scales as shown below,

$$\lambda(x, y) \propto \sum_{i=1}^{N_L} \mathcal{O}\left(\frac{x}{L_i}, \frac{y}{L_i}\right) L_i, \tag{2}$$

where λ is the final two dimensional noise function, L_i is the i^{th} length scale used (listed in Table 1), and N_L is the number of length scales used. The continuous function, $\lambda(x, y)$, is then evaluated on the grid used for each experiment and scaled so that the root mean square (rms) of the discrete noise field is 100 m in all configurations. Each length scale introduces a topographic gradient with a magnitude that is independent of L_i, as demonstrated below,

$$\boldsymbol{\nabla}\lambda(x, y) \propto \sum_{i=1}^{N_L} \boldsymbol{\nabla}\mathcal{O}\left(\frac{x}{L_i}, \frac{y}{L_i}\right). \tag{3}$$

As seen in Figure 3, the maximum displacement caused by the noise field is approximately 300 m and the structure of the continental shelf and other large topographic features is not lost to the noise. In cases where the added noise would create islands in the domain, the noise is locally reduced to keep all topographic features submerged.

In Section 5, we will discuss the important differences between this idealized configuration and the real ocean and assess how the discrepancies may modify the results presented in this article.

3 Experimental setup

The model described in the previous section is computationally very affordable and a wide parameter space can be explored. In total, 53 simulations were conducted with a minimum run time of 220 years. A summary of the experiments is shown in Table 2. There are three sets of experiments: Smooth, Rough, and ACC sensitivity. The Smooth experimental series uses the bathymetry shown in Figure 2a and does not feature any topographic noise. The horizontal resolution is varied from 80 to 10 km and only the 80 and 40 km simulations feature the Gent and McWilliams (1990) eddy parametrization (GM hereafter). The Rough series is exactly the same as the Smooth series but uses topographic noise, as shown in Figure 3, and the horizontal resolution varies from 80 to

Table 2. Summary of the numerical experiments. Resolutions marked with GM use the Gent and McWilliams (1990) eddy parametrization.

	Horizontal resolution (km)					
Experiment series	80^{GM}	40^{GM}	20	10	3	Topographic noise
Smooth	✓	✓	✓	✓	✗	✗
Rough	✓	✓	✓	✓	✓	✓
ACC sensitivity (11 variations of sill height)	✓	✓	✓	✓	✗	✓

3 km. The 3 km simulation is eddy-rich and computationally very expensive so only one eddy-rich time integration could be completed.

In this model the ACC is driven by wind-stress, surface buoyancy forces, and buoyancy forcing on the northern boundary. The ACC transport is not prescribed, so the ACC strength is free to respond to changes in the horizontal resolution. The ACC sensitivity experiment series is designed to assess how strongly the Weddell Gyre and ACC transports are coupled. Not only is a study of the gyre-ACC coupling scientifically interesting; it is also necessary to assess if the changes in the Weddell Gyre transport with resolution are influenced by changes in the idealized ACC strength. In the ACC sensitivity experiments, the height of the Drake Passage sill is varied from 500 m to 2500 m in intervals of 200 m: this modifies the strength of the simulated ACC in a way that does not modify the immediate conditions for the Weddell Gyre. For example, we cannot modify the wind stress to change the ACC strength as this will alter the wind stress curl above the gyre and change the gyre strength directly.

4 Results

As seen in Figure 4, 200 years is a sufficient spin up time to assume a statistically steady Weddell Gyre and ACC transport. Only the gyre transport in the 3 km simulation shows a slight downward trend that does not alter the interpretation of the presented results. All results presented in this section are time-averages taken from the final 20 years of each model run. As shown in Figure 5, the 3 km simulation resolves a rich eddy field in the ACC and the eastern boundary of the zonal ridge. Similar to Wilson et al. (2022), a weaker but qualitatively similar eddy field is partially resolved in 10 and 20 km simulations.

4.1 Transport sensitivity to resolution

In the Rough and Smooth configurations, the Weddell Gyre and ACC are very sensitive to resolution, as shown in Figure 6. Figure 6a shows how the Weddell Gyre transport increases as the resolution is doubled over smooth bathymetry. The time-averaged Weddell Gyre transport is 28.9 Sv in the 80 km simulation and increases to 54.7 Sv in the 10 km simulation. Introducing a rough bathymetry reduces all gyre transports but also increases the Weddell Gyre's sensitivity to resolution (Figure 6c). With a rough bathymetry, the time-averaged Weddell Gyre transport is 11.9 Sv in the 80 km configuration and then rapdily increases to 44.8 Sv in the 10 km configuration. For the Rough configuration, we have access to an eddy-rich simulation where the Weddell Gyre transport is 38.6 Sv. In this case, the transition from an eddy-permitting to an eddy-rich simulation reduces the Weddell Gyre transport by 6.2 Sv.

By studying the stream function of the time-averaged flow in Figure 6, we can see that the gyre shrinks and follows the bathymetry more closely when the resolution in-

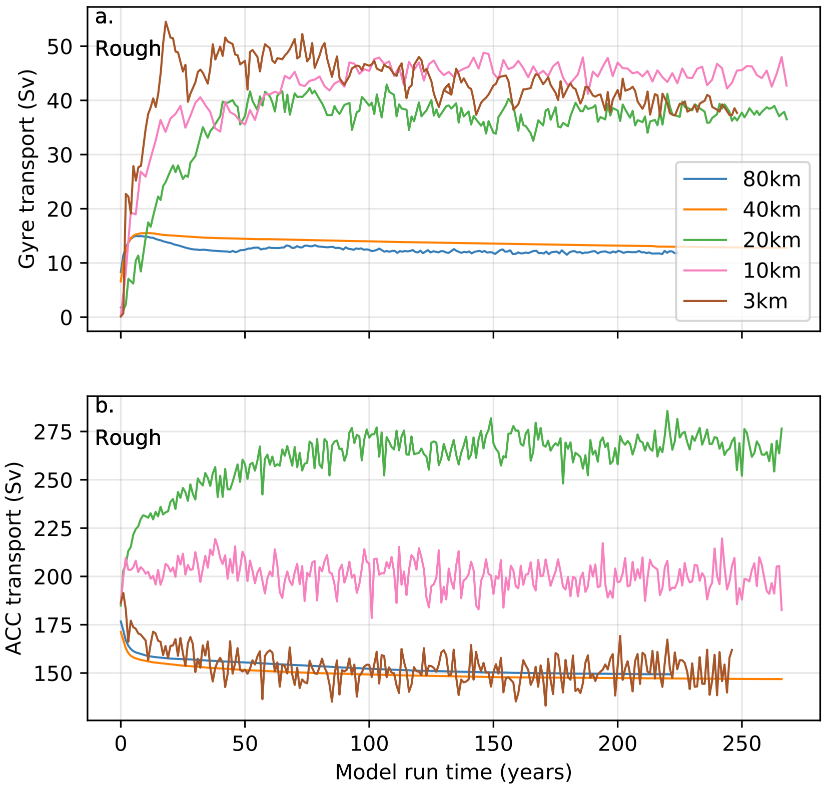

Figure 4. Evolution of the (a) Weddell Gyre and (b) ACC transports for configurations with rough bathymetry. All results presented in this paper are taken from the final 20 years of the model spin up and are in a statistically steady state.

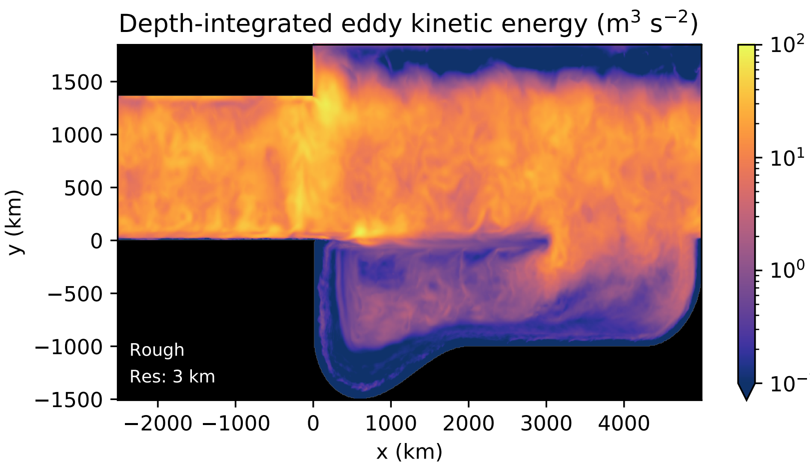

Figure 5. Depth-integrated eddy kinetic energy of the simulation with a 3 km horizontal resolution and rough bathymetry. The color map is logarithmic to show the large range in eddy kinetic energy.

creases from eddy-parametrized (80 km) to eddy-permitting (10 km) scales. The boundary current that forms on the submarine ridge becomes particularly narrow and intense. In Section 4.3 we use a thermal wind decomposition to relate the transports and stream functions shown in Figure 6 to horizontal density gradients and the velocity at the sea floor.

The structure of the ACC is sensitive to the coarseness of the bathymetry. In the Smooth configurations, the ACC deflects northwards by the ridge in the Drake Passage but quickly returns to a zonal flow which results in large positive and negative meridional velocities in the ACC. In the Rough configurations, the northward deflection of the ACC is similarly severe but the topographic noise appears to dampen the ACC's return to a zonal flow. Consequently, we have large positive meridional velocities and comparatively small negative meridional velocities. The ACC's behaviour in the Rough configurations more closely resembles the real behaviour of the ACC east of the Drake Passage.

The time-averaged ACC transport is also very sensitive to resolution in both Smooth and Rough configurations. In particular, the transition from a smooth to rough bathymetry intensifies the ACC transport at eddy-permitting resolutions. The ACC transport will also be related to horizontal density gradients and the bottom velocity in Section 4.3. With a maximum ACC transport of 266.2 Sv (20 km resolution, rough bathymetry) and a minimum of 147.7 Sv (40 km resolution, rough bathymetry), it is important to assess if such large variations in the ACC transport modify the Weddell Gyre transport directly.

4.2 ACC sensitivity results

In the ACC sensitivity experiments, the strength of the ACC is varied by modifying the height of the sill in the idealized Drake Passage. As shown in Table 2, these experiments are at horizontal resolutions ranging from 80 to 10 km and all experiments have a rough bathymetry.

The results of the ACC sensitivity experiment are shown in Figure 7. By comparing the y-axis and x-axis scales in Figure 7 we can immediately see that the gyre transport responds slightly (~ 1 Sv) to large changes in the idealized ACC transport (~ 100 Sv). By comparing Figure 7 to Figure 6, we can see that the large changes in the Weddell Gyre transport with resolution are controlled by the gyre's direct sensitivity to resolution and not the gyre's sensitivity to the ACC strength.

4.3 Thermal wind and bottom flow decomposition

In Section 4.1 we observe that the idealized Weddell Gyre and ACC transports are sensitive to horizontal resolution and are particularly strong at eddy-permitting resolutions. In this section, we relate the observed transports to the isopycnal structure of the circulation and the strength of the circulation at the sea floor. The depth-integrated velocity field is separated into depth-dependent and depth-independent components using integration by parts,

$$\mathbf{U} = \int_{-H}^{\eta} \mathbf{u}\, dz = \mathbf{u}_b H + \mathbf{u}_t \eta - \int_{-H}^{\eta} \frac{\partial \mathbf{u}}{\partial z} z\, dz, \tag{4}$$

where $\mathbf{U}$ is the depth-integrated velocity field, η is the free surface height, $\mathbf{u}_b$ is the velocity at the sea floor, and $\mathbf{u}_t$ is the velocity at the free surface. We then use the following equation to describe how the the velocity field varies with depth,

$$f \frac{\partial \mathbf{u}}{\partial z} = -\frac{g}{\rho_0} \left(\hat{\mathbf{k}} \times \boldsymbol{\nabla}_h \rho \right) + \boldsymbol{\mathcal{E}}, \tag{5}$$

where g is the acceleration due to gravity, ρ_0 is the reference density, $\boldsymbol{\nabla}_h$ is the horizontal gradient operator, ρ is the density, and $\boldsymbol{\mathcal{E}}$ is a residual function. Equation 5 is the ther-

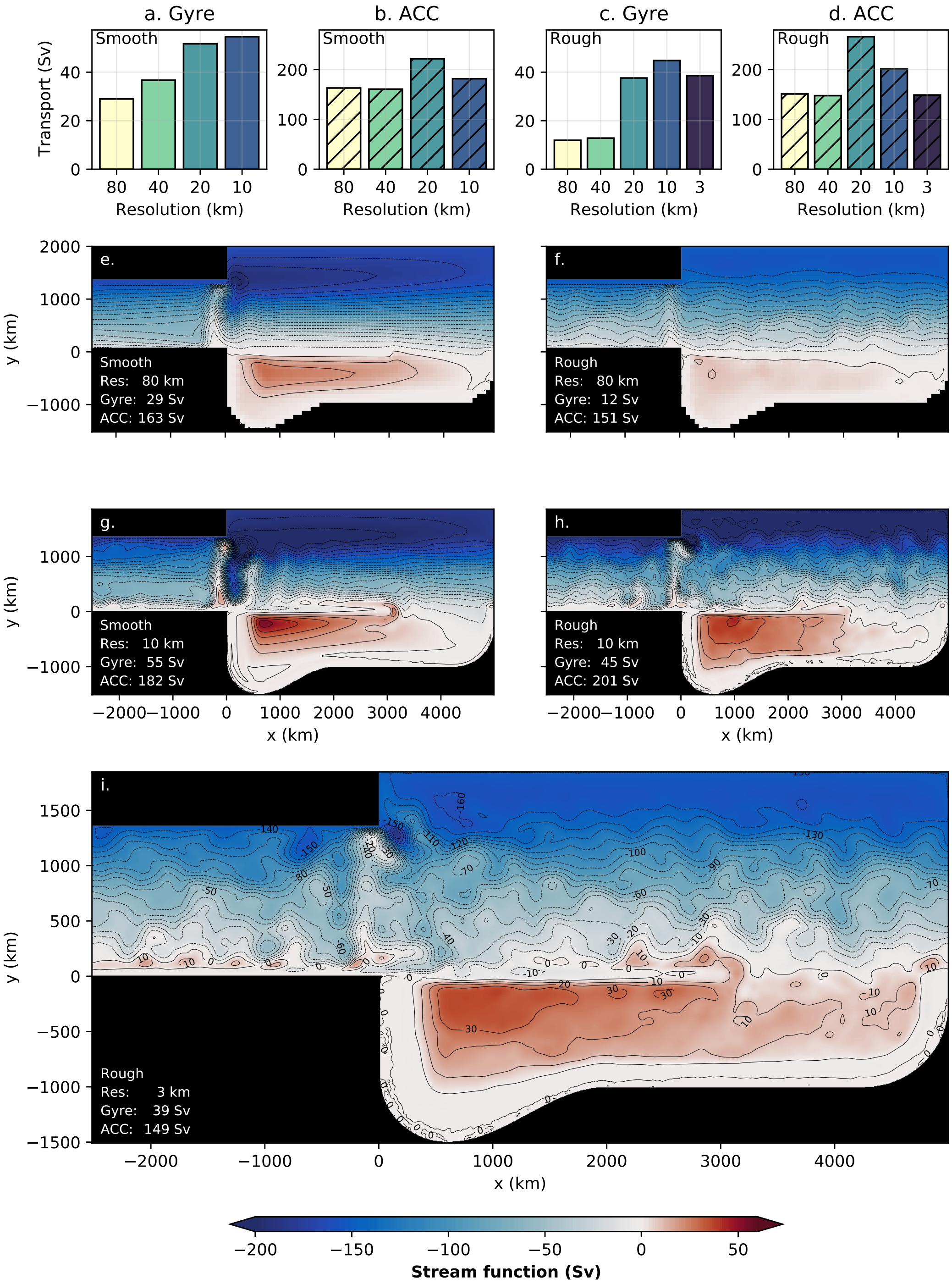

Figure 6. Sensitivity of the Weddell Gyre and ACC transport to resolution. (a)-(d) show the time-averaged gyre and ACC transport over smooth and rough bathymetry. (e)-(i) are the time-averaged stream functions from configurations at an eddy-parametrized resolution (80 km), an eddy-permitting resolution (10 km), and an eddy-rich resolution (3 km).

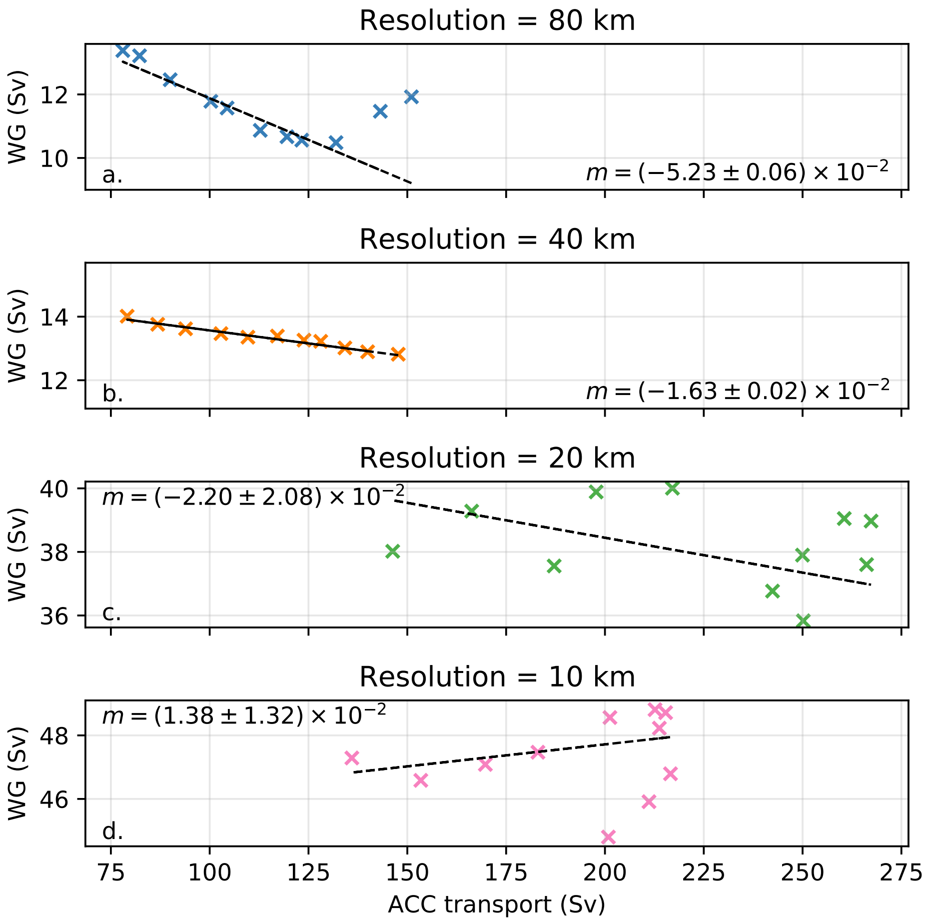

Figure 7. How the Weddell Gyre (WG) transport varies with respect to the ACC transport at several resolutions. The dashed line shows the straight line of best fit and m is the line's dimensionless gradient with error. The gyre transport is very insensitive to large variations in the ACC transport.

mal wind equation where all non-geostrophic terms, non-hydrostatic terms, and numerical errors are aggregated in $\boldsymbol{\mathcal{E}}$. The model used in this article assumes hydrostatic balance so $\boldsymbol{\mathcal{E}}$ is free of non-hydrostatic terms.

By combining Equations 4 and 5 we can derive a full decomposition of the depth-integrated flow,

$$\mathbf{U} = \underbrace{\mathbf{u}_b H}_{\text{Bottom velocity}} + \underbrace{\frac{g}{\rho_0 f}\int_{-H}^{\eta}\left(\hat{\mathbf{k}} \times \boldsymbol{\nabla}_h \rho\right) z \, dz}_{\text{Thermal wind}} + \mathbf{u}_t \eta + \boldsymbol{\mathcal{E}}^z, \tag{6}$$

where $\boldsymbol{\mathcal{E}}^z$ is the depth-integrated and rescaled residual that still contains non-geostrophic terms and errors from the discretization. The free surface term, $\mathbf{u}_t\eta$, is negligible in all of the presented results.

Using Equation 6, we decompose the Weddell Gyre and ACC transport into depth-independent ($\mathbf{u}_b H$) and depth-dependent components (thermal wind and residual). The decomposed transports and the associated stream functions are shown in Figures 8 and 9 respectively. In order to calculate valid stream functions, a Helmholtz decomposition of each term in Equation 6 is calculated using an elliptical solver and the compressible part of the flow is removed. The compressible part of the depth-integrated flow is minor in all cases and is contained in the residual term, $\boldsymbol{\mathcal{E}}^z$. Each component of the gyre transport shown in Figure 8 is equal to the component's stream function evaluated where the gyre's total transport is calculated. The ACC transport components shown are the zonal averages, but zonal variations of the decomposition are small and do not alter our interpretation of the decomposition.

In all cases, the combined transport from the bottom flow and thermal wind component closely describes the total transport of the gyre (black crosses in Figure 8). This suggests that the residual terms are minor when considering the gyre and ACC transports. The circulation associated with the residual term, $\boldsymbol{\mathcal{E}}^z$, is weak across most of the horizontal domain meaning that the depth-integrated circulation can be described to leading order using geostrophic assumptions. It is important to note that a small value of $\boldsymbol{\mathcal{E}}^z$ does not guarantee geostrophy at all depths, but in Section 5.1 we argue that an equivalent deep geostrophic flow closely describes the depth-integrated circulation. The residual is largest at lower resolutions, this may be caused by small departures from geostrophy through viscous effects or a larger numerical error that comes with a coarser grid.

Looking at the gyre transports, the relative significance of the bottom velocity and the thermal wind component depends on the coarseness of the bathymetry. In the Smooth configurations, the bottom velocity plays a dominant role in controlling the gyre transport and increases with horizontal resolution. In configurations with a rough bathymetry, the gyre transport from the bottom flow is reduced and comparable to the thermal wind component, but still increases with resolution. When a rough bathymetry is used, the thermal wind component of the gyre is particularly strong at 10 km resolution and consequently the total gyre transport is particularly strong at eddy-permitting resolutions.

The decomposition of the ACC transport is also dependent on the coarseness of the bathymetry. In simulations with a smooth bathymetry, contributions to the ACC transport from the bottom flow and thermal wind components are similar in size. The bottom flow component shrinks with resolution and the thermal wind component is largest at an eddy-permitting resolution (20 km). When a rough bathymetry is used, the ACC transport is almost entirely determined by the thermal wind component, which is even larger at eddy-permitting resolutions.

The shape of the stream function from the bottom flow and the thermal wind components differ. The thermal wind stream function (left column of Figure 9) features a gyre that lies over the basin interior and submarine ridge and is not west-intensified. Over

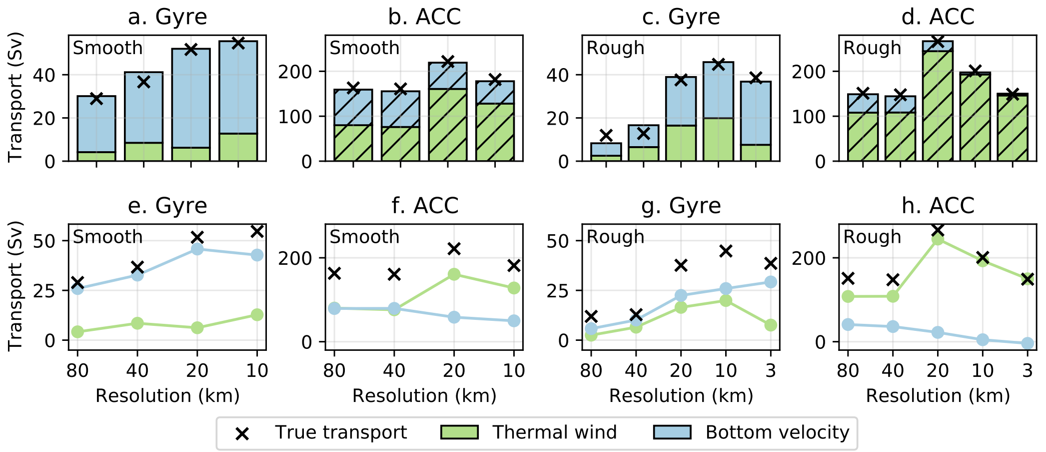

Figure 8. A decomposition of the gyre and ACC transports over smooth and rough bathymetries. The thermal wind component describes the geostrophic transport which emerges from horizontal density gradients. The bottom velocity component describes the depth-independent transport which is determined by the velocity at the sea floor ($u_b H$). The black crosses mark the total gyre and ACC transports shown in Figure 6.

the continental shelf there is a density-driven slope current that reverses direction south of the submarine ridge, which is a consequence of the idealized model design. An accurate slope current may require a wind stress that follows the continental shelf (Thompson et al., 2018) and deep passages in the submarine ridge to allow for deep water export. The stream function for the bottom flow transport (right column of Figure 9) features a gyre that follows the bathymetry closely and is west-intensified. The submarine ridge blocks the deep current but the bottom flow is free to extend northwards into the ACC channel once it is far enough east.

Over the submarine ridge the thermal wind and bottom velocity stream functions reinforce each other, resulting in a particularly strong western and northern boundary current. In contrast the thermal wind and bottom velocity stream function are opposite-signed on the continental shelf, which limits the gyre's presence over the continental shelf in all simulations. In higher resolution simulations, the bottom velocity stream functions uniquely feature intense recirculations to the east of the Drake Passage.

4.4 Sensitivity of the thermal wind component to resolution

In the previous section we note that the depth-varying component of the flow can be closely described by the thermal wind relation and ultimately related to horizontal density gradients. To understand why the thermal wind component of the gyre and the ACC is particularly strong at eddy-permitting resolutions, we study the isopycnal structure at various resolutions. Zonal averages of the density over five meridional sections are presented over the Channel (-2000 $< x <$ -1000 m), West Ridge (500 $< x <$ 1000 m), East Ridge (2000 $< x <$ 2500 m), East of the ridge (3500 $< x <$ 4000 m), and the Full Zonal Average.

Figure 10 compares the isopycnal structure between an eddy-permitting (10 km) and an eddy-parametrized (80 km) simulation with rough bathymetry. The isopycnal structure for simulations with a smooth bathymetry are qualitatively similar. In all meridional sections, we can see that the isopycnals are more tilted in the eddy-permitting simulation. In particular, meridional density gradients over the submarine ridge are very

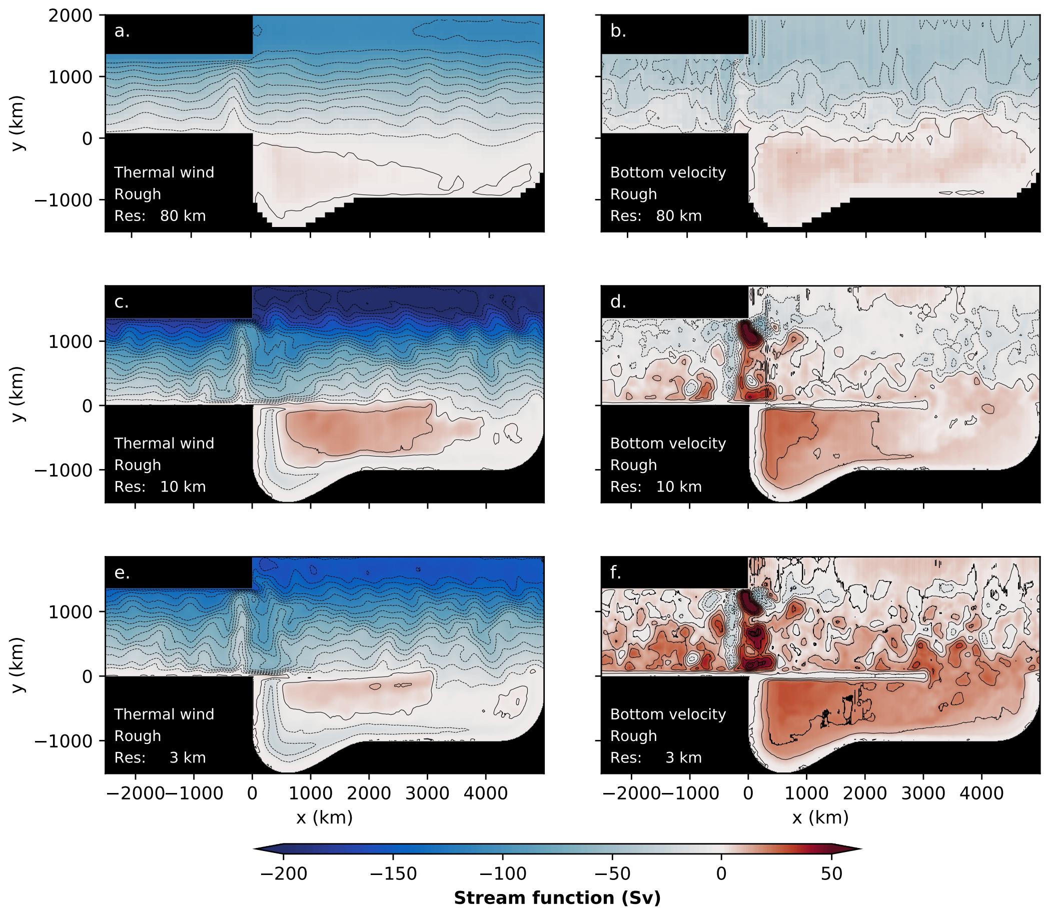

Figure 9. Stream functions from the same decomposition shown in Figure 8 at various resolutions. Results are from configurations with a rough bathymetry. The combined thermal wind and bottom velocity stream function is approximately equal to the total stream function, shown in Figure 6.

large at eddy-permitting resolutions and the stratification of the gyre basin ($y < 0$) is reduced. Our results agree with the findings of Wilson et al. (2022) as the submarine ridge plays a large role in setting the model stratification at eddy-permitting resolutions. From Figure 10 we can conclude that the thermal wind component of the gyre and ACC transports is larger in eddy-permitting models as density gradients are more extreme in the upper 2000 m of the model. A thick and weakly stratified layer also emerges in the eddy-permitting simulations, which is approximately below the 1028.5 kg m^{-3} contour. In this layer, horizontal density gradients are small and the thermal wind relation suggests that the zonal flow is not expected to vary significantly with depth.

Figure 11 compares the isopycnal structure between an eddy-rich (3 km) and the same eddy-permitting (10 km) simulation with rough bathymetry. The isopycnals of the eddy-rich and eddy-permitting simulations share similar features, however meridional density gradients are smaller in the eddy-rich case. This is particularly noticeable above the submarine ridge and ultimately reduces the thermal wind transport of the gyre and ACC in the upper 2000 m of the model. The reduced outcropping of isopycnals in the eddy-rich model also increases the stratification of the gyre basin and reduces the thickness of the weakly stratified layer (approximately below 1028.5 kg m^{-3} contour).

Such large horizontal density gradients are uncommon in eddy-parametrized models. For numerical stability, eddy-parametrized models (80 and 40km) feature the strongest tracer diffusion terms and eddy schemes like the GM parametrization simulate the effect of unresolved eddies by flattening isopycnals. In the presented simulations (and many climate models), the diffusion parameters and the parametrized eddies are insensitive to topographic features and consequently the isopycnals are relatively flat over the submarine ridge and the gyre basin. The eddy-permitting simulations are significantly less diffusive and no eddy-parametrization is used. The partially resolved eddy field is insufficient to flatten the isopycnals to the same extent as the eddy-parametrized models and therefore more extreme density gradients emerge. In the eddy-rich simulation (3 km), diffusive terms are very small, but the near-resolved mesoscale eddy field is able to flatten the density surfaces more effectively than the partially-resolved eddy field.

5 Discussion

In the previous section, we related the thermal wind component of the gyre and ACC transports to the density structure. In contrast, it is not immediately clear why the transport from the bottom flow can vary significantly with resolution. To explore this sensitivity of the bottom flow to resolution, we first consider linear, planetary geostrophic dynamics. We then discuss the potential contributions of non-linear eddy-mean flow interactions. Finally, we will discuss other physical processes neglected in our idealized model.

5.1 Planetary geostrophic dynamics

Consider the case of a planetary geostrophic ocean with a prescribed surface wind stress, $\boldsymbol{\tau}$. The ocean extends from the sea floor at $z = -H(x, y)$, to a rigid lid at $z = 0$. The flow is in exact geostrophic balance, with the addition of a surface Ekman layer. Taking the curl of the momentum equation and integrating over depth, we can derive the linear vorticity equation:

$$\beta\,(V - v_b H) + H^2 \mathbf{u_b} \cdot \boldsymbol{\nabla}(f/H) = (\boldsymbol{\nabla} \times \boldsymbol{\tau}) \cdot \hat{\mathbf{k}}. \tag{7}$$

Here, V is the depth-integrated meridional velocity, v_b is the meridional velocity at the sea floor, and $\mathbf{u_b}$ is the full velocity at the sea floor. A similar equation, involving equivalent Ekman pumping rather than the curl of the wind stress, is derived in D. Marshall (1995). The first term on the left hand side of Equation 7 is the advection of planetary vorticity by the depth-varying component of the flow, relative to the sea floor, and the

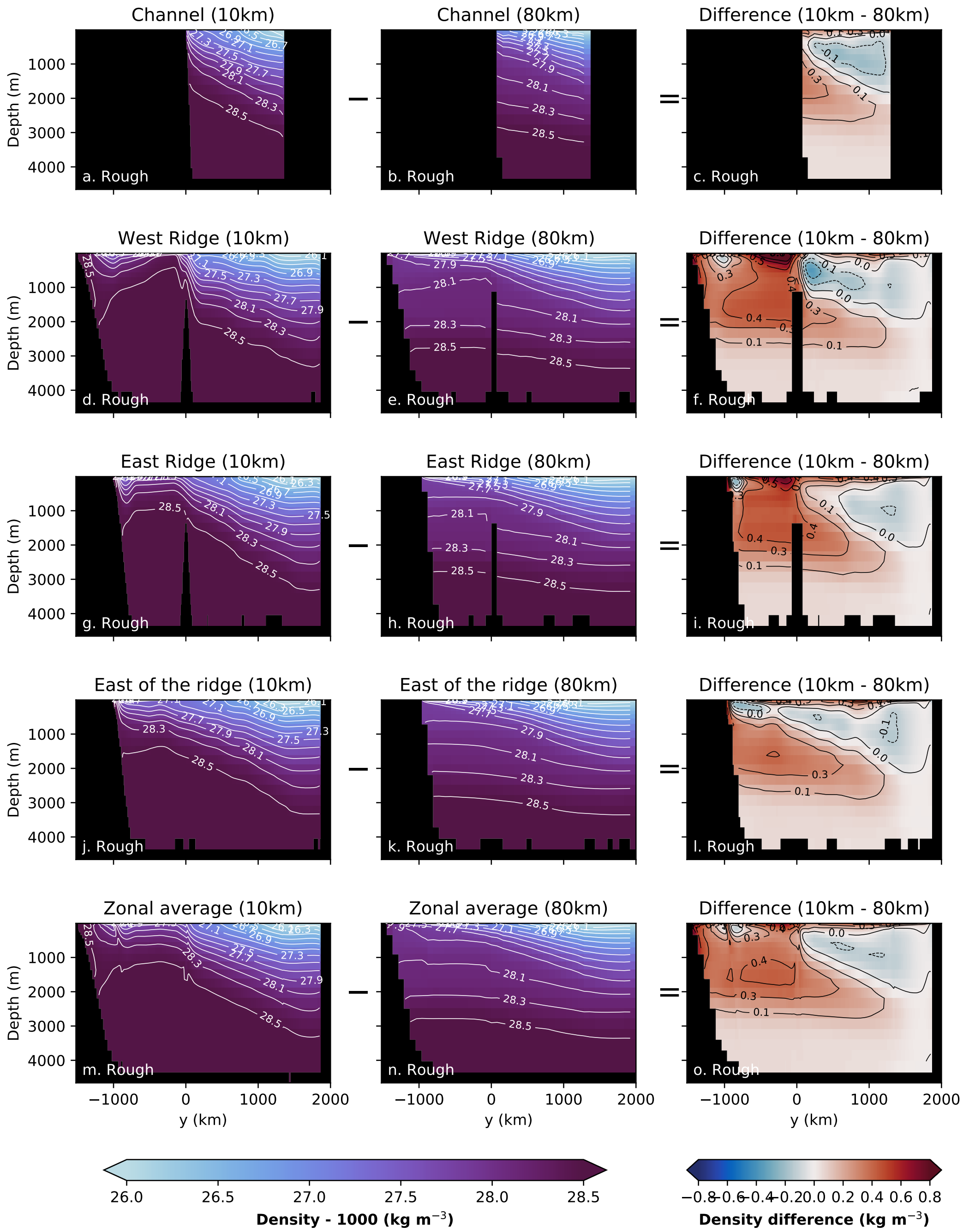

Figure 10. Meridional density sections of an eddy-permitting (10 km, left column) and an eddy paramaterized (80 km, middle column) simulation. The difference between the density sections are shown in the right column. All presented sections feature a rough bathymetry.

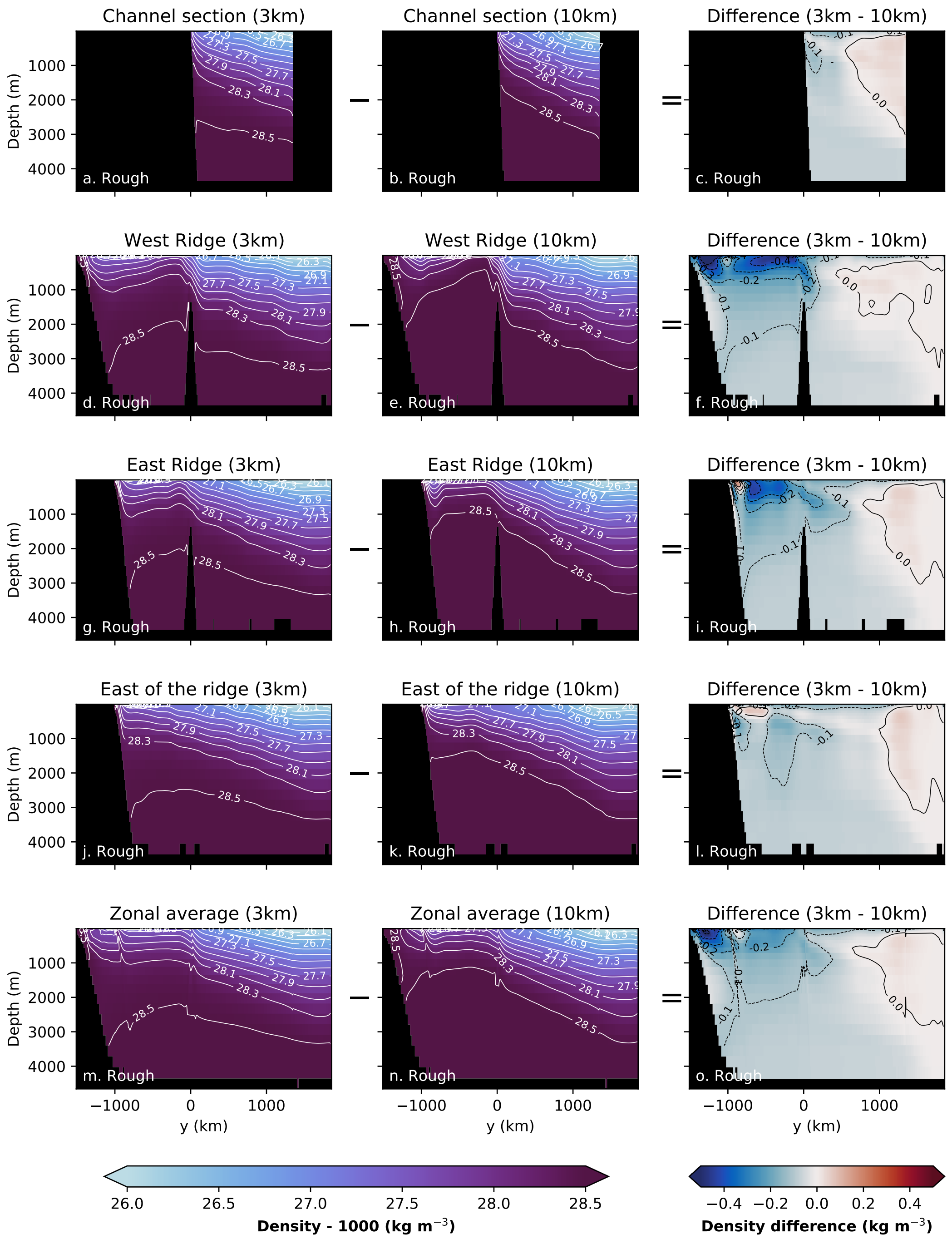

Figure 11. Meridional density sections of an eddy-rich (3 km, left column) and an eddy-permitting (10 km, middle column) simulation. The difference between the density sections are shown in the right column. All presented sections feature a rough bathymetry.

second term is the advection of f/H by the bottom flow. In the absence of the latter term, Equation 7 reduces to Sverdrup balance (e.g. Vallis, 2017).

The last term in Equation 7 constrains the component of the bottom flow that crosses f/H contours. In all of our experiments, the large-scale f/H contours are open, as is the case in the Weddell basin, so the bottom flow is required to cross the f/H contours at some point. In both our model and the ocean, this occurs primarily in the eastern limb of the gyre where the large-scale bathymetry is flat and the southward bottom flow crosses the near-zonal f/H contours.

In our experiments, the sign of both terms on the left hand side of Equation 7 is negative in the eastern limb of the gyre (not shown). This implies that an increase in the depth-varying flow, relative to the sea floor, should be compensated by a decrease in the bottom flow. This is not what we observe in our experiments (see Figure 8). The corollary is that non-linear dynamics is necessary to reconcile our results.

5.2 Role of eddies

In this article, we observe that the density surfaces of the idealized Weddell Gyre change significantly when explicit eddies are introduced to ocean simulations and that the density structure has a significant influence on the horizontal circulation. In the presence of rough bathymetry, the thermal wind component of the gyre transport intensifies in simulations with explicit eddies because the meridional density gradients are steeper. In turn, the increase in the mean available potential energy that comes with steeper isopycnals may fuel more energetic mesoscale eddies. In Figure 5, we can see that eddies are particularly prominent to the east of the zonal submarine ridge, where the isopycnal tilt is much larger than the eddy-parametrized case (see Figure 10j and Figure 10k).

In the presence of variable bottom topography, mesoscale eddies can drive a mean circulation along topographic contours (Bretherton & Haidvogel, 1976). This can be interpreted either as an 'entropic force' (Holloway, 1987, 1992) or, alternatively, as energetically constrained mixing of potential vorticity over the sloping topography (Bretherton & Haidvogel, 1976; Adcock & Marshall, 2000). These eddy-driven flows are not captured by eddy parametrizations employed in climate models based on GM. However, it is possible that these entropic forces are captured in our simulations with explicit eddies, consistent with the strengthening of the bottom flow at higher resolutions. This deserves further investigation, but is beyond the scope of the present study.

As eddy-permitting models become more feasible for climate projections, there is an increasing interest in developing eddy parametrizations for simulations where the largest eddies are at least marginally resolved. The development and testing of eddy parametrizations is a busy area of research; Hewitt et al. (2020) reviews the various approaches that could be deployed in eddy-parametrized and eddy-permitting ocean models. Of particular relevance to the Weddell gyre is a recent study by Wei et al. (2022) which finds encouraging results for parametrized mesoscale eddy buoyancy fluxes over large scale bathymetry when topographic suppression effects are incorporated.

5.3 Missing physics in the idealized configuration

Before concluding on the results presented in this article, it is important to summarize the limitations of the idealized model. Firstly, the winds in these configurations are zonal and do not follow the continental shelf. This may be the reason why the density driven slope current in this model does not reach the Drake Passage; additionally, a complete slope current may require deep passages in the zonal submarine ridge. Presently, it is unclear if a more accurate slope current would modify the gyre transport significantly.

We imitate the time-averaged effect of ice with an effective freshwater flux shown in Figure 2d but no attempt is made to couple the effect of sea ice to the oceanic or atmospheric state. In addition, the effect of internal stresses in the ice can modify the surface stress experience by the ocean. By neglecting internal stresses, we are assuming that all ice is in 'free drift' which may not be valid near the continental shelf according to satellite observations (Kimura, 2004; Kwok et al., 2017).

In reality, the Weddell Gyre and ACC are exposed to an extreme seasonal cycle. The amplitude of the time-averaged wind stress and buoyancy forcing is, at most, comparable to the amplitude of the seasonal cycle. In this work we are assuming that time-averaged forcing will accurately produce a time-averaged Weddell Gyre and ACC, but this may not be true because of non-linear processes. This is certainly not true for the subpolar gyres in the northern hemisphere, where winter conditions play a disproportionately large role in setting the properties of the deep ocean thermocline as waters subducted at any time outside of late-winter are re-entrained by the dynamic mixed layer (Stommel, 1979). A similar mechanism also operates on an inter-annual time scale in the northern hemisphere (MacGilchrist et al., 2021). It is unclear if a similar selection process ('Stommel's Demon') is present in the Southern Ocean and needs further investigation. It should also be noted that all experiments used in this study are in a statistically steady state (see Figure 4), unlike the real ocean which is exposed to an extreme seasonal cycle, a changing global ocean, and a changing climate.

The large-scale topographic features in the model (shown in Figure 2a) are qualitatively similar to the Weddell basin but there are some important differences. Firstly, the submarine ridge and the northern boundary of the domain are zonal. The meridional components of the idealized Weddell Gyre and ACC are too constrained by bottom topography when compared to the real ocean. In reality, the ACC is deflected northwards immediately upon exiting the Drake Passage which is a behaviour this idealized model cannot recreate. Finally, a unique feature of the Weddell Gyre is its dynamic shape as no obvious topographic feature constrains the gyre's eastern boundary. In our idealized simulations, the zonal extent of the Weddell Gyre is not able to extend beyond the width of the basin (5000 km) without taking a northward departure into the ACC channel.

6 Conclusions

Using a minimal description of the Weddell Gyre and ACC, we have identified an extreme sensitivity of the circulation to horizontal grid spacing between eddy-parametrized and eddy-permitting resolutions. The Weddell Gyre in eddy-permitting simulations is significantly stronger than the same gyre in eddy-parametrized cases and slightly stronger than an eddy-rich case. This is concerning as coupled climate models are beginning to traverse this highly sensitive 'gray zone', where large mesoscale eddies are only partially resolved.

To investigate if the gyre transports are affected by the varying ACC strength, we performed a sensitivity experiment. The channel topography was modified to either increase or decrease the ACC transport at eddy-parametrized and eddy-permitting resolutions and the effect on the Weddell Gyre was negligible. This was useful for our study as we do not have to consider the ACC-gyre transport connectivity but the insensitivity itself is also scientifically interesting and should be investigated further.

To improve our understanding of the flow's vertical structure, we used a thermal wind decomposition which works well with a small residual. In cases with a smooth bathymetry, the gyre strength is almost entirely determined by the depth-independent, bottom flow transport, $u_b H$. When a rough bathymetry is used, the bottom gyre transport is comparable in size to the thermal wind transport, which varies with depth. Although the total transport sensitivity to resolution is similar with smooth and rough bathymetry, the vertical and horizontal structure of the flow clearly differs. This highlights how permitting small topographic interactions everywhere in an idealized model can change large scale circulation features.

With a rough bathymetry, the thermal wind component of the gyre is particularly large at eddy-permitting resolutions, especially over the submarine ridge. This is a consequence of the partially-resolved eddy field being less effective at flattening isopycnals than a fully-resolved eddy field or an eddy parametrization. In all cases, the bottom flow transport of the gyre increases significantly when explicit eddies are present. This sensitivity cannot be explained by linear planetary geostrophic dynamics so non-linear dynamics are necessary to reconcile our results.

In this study, the Weddell Gyre transport is largest and the isopycnals are the steepest at eddy-permitting resolutions. For this reason, ocean modellers should approach this eddy-permitting 'gray zone' with care when simulating the Southern Ocean and consider employing parametrizations that are compatible with partially resolved mesoscale eddies.

Acknowledgments

This work was financially supported by the Natural Environment Research Council NE/S007474/1. Mike Bell was supported by the Met Office Hadley Centre Climate Programme funded by BEIS and Defra and funding for the Met Office's Public Weather Service. This work used Monsoon2, a collaborative High-Performance Computing facility funded by the Met Office and the Natural Environment Research Council. This work also used the ARCHER2 UK National Supercomputing Service (`https://www.archer2.ac.uk`) and JASMIN, the UK collaborative data analysis facility.

Input files for the idealized model integrations are archived on Zenodo (Styles et al., 2023). The idealized configuration, designed for NEMO release 4.0.1, is available from `https://github.com/afstyles/IdealisedWeddellGyre/tree/b59c815`. The software used to analyse the model outputs is available from `https://github.com/afstyles/IWG_analysis/tree/b3aae7a`

References

Adcock, S. T., & Marshall, D. P. (2000, December). Interactions between Geostrophic Eddies and the Mean Circulation over Large-Scale Bottom Topography. *Journal of Physical Oceanography*, *30*(12), 3223–3238. doi: 10.1175/1520-0485(2000)030⟨3223:IBGEAT⟩2.0.CO;2

Argo. (2020). *Argo float data and metadata from Global Data Assembly Centre (Argo GDAC).* https://www.seanoe.org/data/00311/42182/. doi: 10.17882/42182

Armitage, T. W. K., Kwok, R., Thompson, A. F., & Cunningham, G. (2018, January). Dynamic Topography and Sea Level Anomalies of the Southern Ocean: Variability and Teleconnections. *Journal of Geophysical Research: Oceans*, *123*(1), 613–630. doi: 10.1002/2017JC013534

Bretherton, F. P., & Haidvogel, D. B. (1976, November). Two-dimensional turbulence above topography. *Journal of Fluid Mechanics*, *78*(1), 129–154. doi: 10.1017/S002211207600236X

Deacon, G. E. R. (1979, September). The Weddell gyre. *Deep Sea Research Part A. Oceanographic Research Papers*, *26*(9), 981–995. doi: 10.1016/0198-0149(79)90044-X

Fahrbach, E., Knoche, M., & Rohardt, G. (1991, November). An estimate of water mass transformation in the southern Weddell Sea. *Marine Chemistry*, *35*(1-4), 25–44. doi: 10.1016/S0304-4203(09)90006-8

Fox-Kemper, B. (2018, August). Notions for the Motions of the Oceans. In E. P. Chassignet, A. Pascual, J. Tintoré, & J. Verron (Eds.), *New Frontiers in Operational Oceanography.* GODAE OceanView. doi: 10.17125/gov2018.ch02

Gent, P. R., & McWilliams, J. C. (1990). Isopycnal Mixing in Ocean Circulation Models. *Journal of Physical Oceanography*. doi: 10.1175/1520-0485(1990)020⟨0150:imiocm⟩2.0.co;2

Gordon, A. L., Martinson, D. G., & Taylor, H. W. (1981). The wind-driven circulation in the Weddell-Enderby Basin. *Deep Sea Research Part A, Oceanographic Research Papers*, *28*(2), 151–163. doi: 10.1016/0198-0149(81)90087-X

Hewitt, H. T., Roberts, M., Mathiot, P., Biastoch, A., Blockley, E., Chassignet, E. P., ... Zhang, Q. (2020, December). Resolving and Parameterising the Ocean Mesoscale in Earth System Models. *Current Climate Change Reports*, *6*(4), 137–152. doi: 10.1007/s40641-020-00164-w

Holloway, G. (1987, November). Systematic forcing of large-scale geophysical flows by eddy-topography interaction. *Journal of Fluid Mechanics*, *184*, 463–476. doi: 10.1017/S0022112087002970

Holloway, G. (1992, September). Representing Topographic Stress for Large-Scale Ocean Models. *Journal of Physical Oceanography*, *22*(9), 1033–1046. doi: 10.1175/1520-0485(1992)022⟨1033:RTSFLS⟩2.0.CO;2

Jullion, L., Garabato, A. C. N., Bacon, S., Meredith, M. P., Brown, P. J., Torres-Valdés, S., ... Fahrbach, E. (2014). The contribution of the Weddell Gyre to the lower limb of the Global Overturning Circulation. *Journal of Geophysical Research: Oceans*, *119*(6), 3357–3377. doi: 10.1002/2013JC009725

Kimura, N. (2004, August). Sea Ice Motion in Response to Surface Wind and Ocean Current in the Southern Ocean. *Journal of the Meteorological Society of Japan. Ser. II*, *82*(4), 1223–1231. doi: 10.2151/JMSJ.2004.1223

Kwok, R., Pang, S. S., & Kacimi, S. (2017, January). Sea ice drift in the Southern Ocean: Regional patterns, variability, and trends. *Elementa*, *5*. doi: 10.1525/ELEMENTA.226/112431

LaCasce, J. H., & Groeskamp, S. (2020, September). Baroclinic Modes over Rough Bathymetry and the Surface Deformation Radius. *Journal of Physical Oceanography*, *50*(10), 2835–2847. doi: 10.1175/JPO-D-20-0055.1

MacGilchrist, G. A., Johnson, H. L., Lique, C., & Marshall, D. P. (2021). Demons in the North Atlantic: Variability of Deep Ocean Ventilation. *Geophysical Research Letters*, *48*(9), 1–9. doi: 10.1029/2020GL092340

Madec, G., Bourdallé-Badie, R., Chanut, J., Samson, E. C., Coward, A., Ethé, C., ... Samson, G. (2019, October). *NEMO ocean engine.* Zenodo. doi: 10.5281/zenodo.1464816

Marshall, D. (1995). Influence of Topography on the Large-Scale Ocean Circulation. *Journal of Physical Oceanography*. doi: 10.1175/1520-0485(1995)025⟨1622:iototl⟩2.0.co;2

Marshall, J., & Speer, K. (2012, March). Closure of the meridional overturning circulation through Southern Ocean upwelling. *Nature Geoscience*, *5*(3), 171–180. doi: 10.1038/ngeo1391

Meijers, A. J., Meredith, M. P., Abrahamsen, E. P., Morales Maqueda, M. A., Jones, D. C., & Naveira Garabato, A. C. (2016). Wind-driven export of Weddell Sea slope water. *Journal of Geophysical Research: Oceans*. doi: 10.1002/2016JC011757

Orsi, A. H., Johnson, G. C., & Bullister, J. L. (1999, January). Circulation, mixing, and production of Antarctic Bottom Water. *Progress in Oceanography*, *43*(1), 55–109. doi: 10.1016/S0079-6611(99)00004-X

Orsi, A. H., Nowlin, W. D., & Whitworth, T. (1993, January). On the circulation and stratification of the Weddell Gyre. *Deep Sea Research Part I: Oceanographic Research Papers*, *40*(1), 169–203. doi: 10.1016/0967-0637(93)90060-G

Orsi, A. H., Smethie Jr., W. M., & Bullister, J. L. (2002). On the total input of

Antarctic waters to the deep ocean: A preliminary estimate from chlorofluorocarbon measurements. *Journal of Geophysical Research: Oceans*, *107*(C8), 31-1-31-14. doi: 10.1029/2001JC000976

Orsi, A. H., Whitworth, T., & Nowlin, W. D. (1995, May). On the meridional extent and fronts of the Antarctic Circumpolar Current. *Deep Sea Research Part I: Oceanographic Research Papers*, *42*(5), 641–673. doi: 10.1016/0967-0637(95)00021-W

Park, Y.-H., Charriaud, E., Craneguy, P., & Kartavtseff, A. (2001). Fronts, transport, and Weddell Gyre at 30°E between Africa and Antarctica. *Journal of Geophysical Research: Oceans*, *106*(C2), 2857–2879. doi: 10.1029/2000JC900087

Pellichero, V., Sallée, J. B., Chapman, C. C., & Downes, S. M. (2018). The southern ocean meridional overturning in the sea-ice sector is driven by freshwater fluxes. *Nature Communications*, *9*(1), 1–9. doi: 10.1038/s41467-018-04101-2

Reeve, K. A., Boebel, O., Strass, V., Kanzow, T., & Gerdes, R. (2019). Horizontal circulation and volume transports in the Weddell Gyre derived from Argo float data. *Progress in Oceanography*, *175*(August 2017), 263–283. doi: 10.1016/j.pocean.2019.04.006

Ryan, S., Schröder, M., Huhn, O., & Timmermann, R. (2016, January). On the warm inflow at the eastern boundary of the Weddell Gyre. *Deep Sea Research Part I: Oceanographic Research Papers*, *107*, 70–81. doi: 10.1016/j.dsr.2015.11.002

Schröder, M., & Fahrbach, E. (1999, January). On the structure and the transport of the eastern Weddell Gyre. *Deep Sea Research Part II: Topical Studies in Oceanography*, *46*(1), 501–527. doi: 10.1016/S0967-0645(98)00112-X

Spencer, K. (2022, October). *OpenSimplex Noise.* Retrieved from `https://github.com/lmas/opensimplex`

Stommel, H. (1979). Determination of water mass properties of water pumped down from the Ekman layer to the geostrophic flow below. *Proceedings of the National Academy of Sciences*, *76*(7), 3051–3055. doi: 10.1073/pnas.76.7.3051

Styles, A. F., Bell, M. J., & Marshall, D. P. (2023). *Data for "The Sensitivity of an Idealized Weddell Gyre to Horizontal Resolution".* Zenodo. doi: 10.5281/zenodo.7602478

Thompson, A. F., Stewart, A. L., Spence, P., & Heywood, K. J. (2018). The Antarctic Slope Current in a Changing Climate. *Reviews of Geophysics*, *56*(4), 741–770. doi: 10.1029/2018RG000624

Vallis, G. K. (2017). *Atmospheric and oceanic fluid dynamics: Fundamentals and large-scale circulation, second edition.* doi: 10.1017/9781107588417

Vernet, M., Geibert, W., Hoppema, M., Brown, P. J., Haas, C., Hellmer, H. H., … Verdy, A. (2019). The Weddell Gyre, Southern Ocean: Present Knowledge and Future Challenges. *Reviews of Geophysics*, *57*(3), 623–708. doi: 10.1029/2018RG000604

Wang, Z. (2013). On the response of Southern Hemisphere subpolar gyres to climate change in coupled climate models. *Journal of Geophysical Research: Oceans*, *118*(3), 1070–1086. doi: 10.1002/jgrc.20111

Wei, H., Wang, Y., Stewart, A. L., & Mak, J. (2022). Scalings for Eddy Buoyancy Fluxes Across Prograde Shelf/Slope Fronts. *Journal of Advances in Modeling Earth Systems*, *14*(12), e2022MS003229. doi: 10.1029/2022MS003229

Wilson, E. A., Thompson, A. F., Stewart, A. L., & Sun, S. (2022, February). Bathymetric Control of Subpolar Gyres and the Overturning Circulation in the Southern Ocean. *Journal of Physical Oceanography*, *52*(2), 205–223. doi: 10.1175/JPO-D-21-0136.1

Yaremchuk, M., Nechaev, D., Schroter, J., & Fahrbach, E. (1998). A dynamically consistent analysis of circulation and transports in the southwestern Weddell Sea. *Annales Geophysicae*, *16*(8), 1024–1038. doi: 10.1007/s00585-998-1024-7